

Volatile Organic Compound Detection Using Insect Odorant-Receptor Functionalised Field-Effect Transistors

by

Eddyn Oswald Perkins Treacher

A thesis submitted in fulfilment of the
requirements of the degree of
Doctor of Philosophy in Physics
School of Physical and Chemical Sciences
Te Herenga Waka - Victoria University of Wellington

Sep 2023



Acknowledgements

69450

Rifat, Alex - vapour sensor Erica Cassie - FET sensing setup Rob Keyzers and Jennie Ramirez-Garcia - NMR spectra Patricia Hunt - Computational chemistry

1. Characteristics of Pristine Carbon Nanotube & Graphene Field Effect Transistors

103704

1.1. Carbon Nanotube Network Morphology

Figure 1.1 shows a side-by-side comparison of the surface morphology of carbon nanotube films fabricated using the methods described in **?@sec-dep-carbon-nanotubes**. These images were collected using an atomic force microscope and processed in the manner described in **?@sec-afm-characterisation**. They each show bundles of carbon nanotubes with a range of diameters and lengths, with each bundle containing one or multiple nanotubes. As discussed in previous works using solvent-based deposition techniques for depositing carbon nanotubes, multi-tube bundles form due to strong mutual attraction between nanotubes [1]–[4]. However, when surfactants are present, they adsorb onto the carbon nanotubes and form a highly repulsive structure able to overcome the strong attraction between nanotubes. This repulsion then keeps the individual carbon nanotubes isolated [5], [6]. The diameter range provided by the supplier for the individual carbon nanotubes used is 1.2–1.7 nm, while the length range is 0.3–5.0 μm (Nanointegris).

The distribution of the deposited carbon nanotubes was modelled to quantitatively understand the effect of the various methods used on the resulting network morphology. The diameter range of deposited single-walled carbon nanotubes can be modelled via a normal or Gaussian distribution [2], [7], [8]. However, when we extract and bin the height profiles from the 2.5 μm x 2.5 μm AFM images in Figure 1.1, the histograms do not follow a normal distribution. The AFM histogram shape results from the SiO_2 substrate and carbon nanotubes both exhibiting a degree of surface roughness, which is partially due to the presence of atmospheric contaminants. In the case of the surfactant-deposited networks, residual surfactant may also contribute to surface roughness [8].

It has been demonstrated that the surface roughness of a bare SiO_2 substrate can also be modelled with a normal distribution. This normal distribution has a spread of approximately ± 1 nm about the mean, which can be set as the reference or zero point for other height measurements [9]. As both the carbon nanotube and silicon dioxide background heights can each be modelled using a normal distribution, we therefore assume that a

1. *Characteristics of Pristine Carbon Nanotube & Graphene Field Effect Transistors*

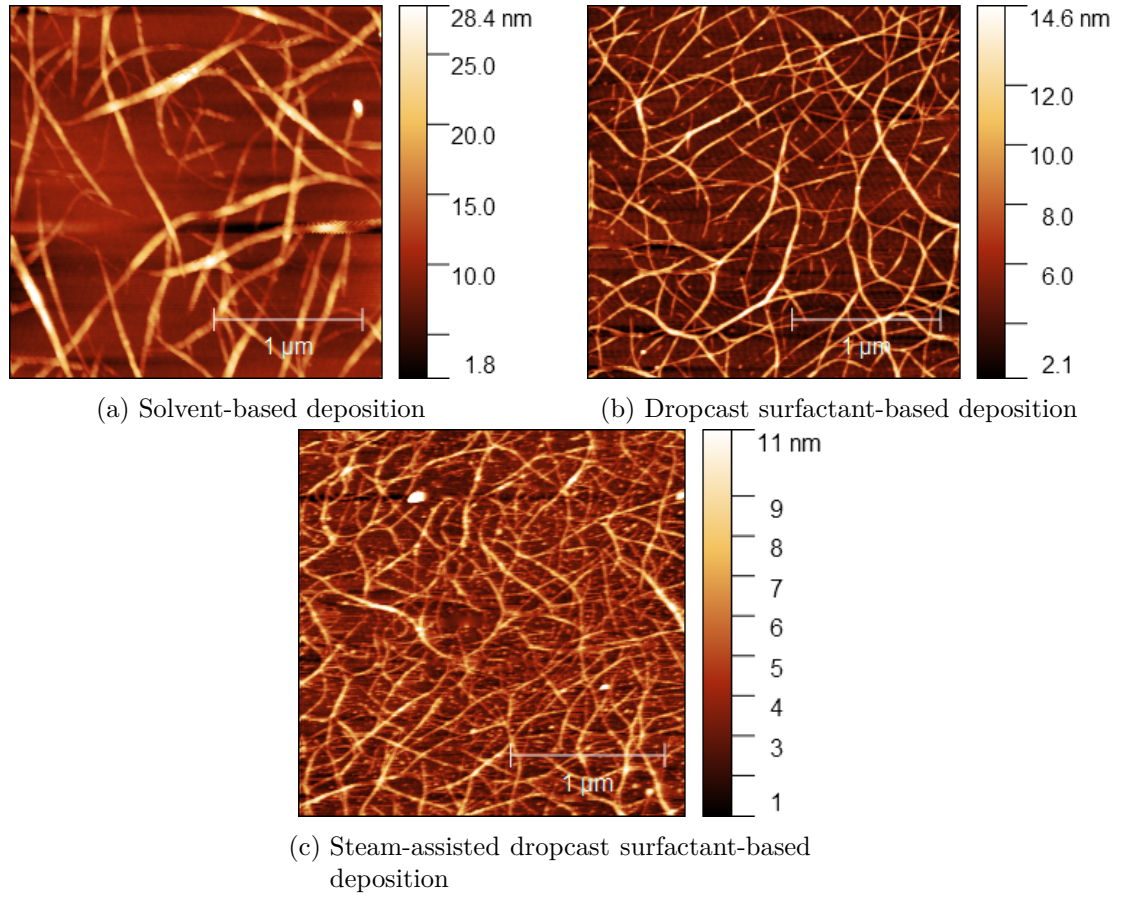


Figure 1.1.: $2.5\ \mu\text{m} \times 2.5\ \mu\text{m}$ atomic force microscope images of carbon nanotube films deposited using various methods. NOTE NEED TO ADD EXAMPLES OF SURFACTANT BASED DEPOSITION POST-ANNEALLING!!!

linear combination of normal distributions can be used to model the AFM histograms in Figure 1.1.

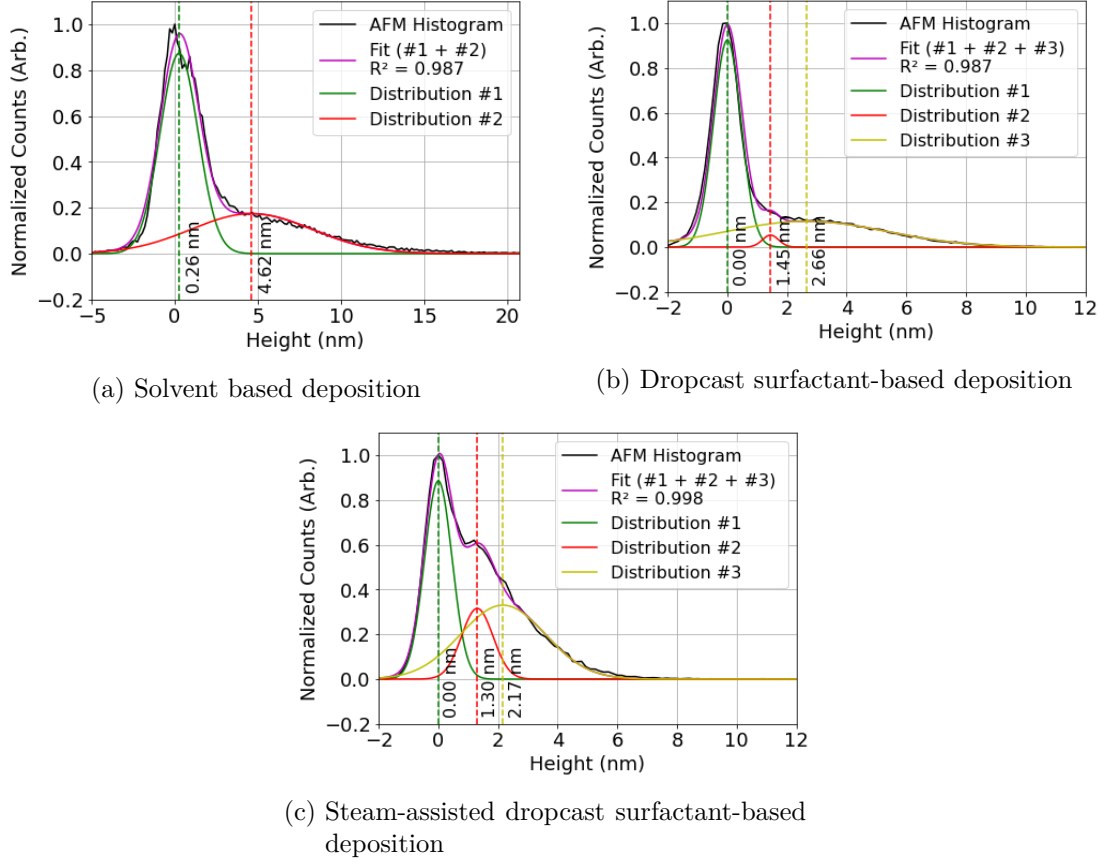


Figure 1.2.: Surface profile histograms extracted from the $2.5 \mu\text{m} \times 2.5 \mu\text{m}$ atomic force microscope images seen in Figure 1.1, each fitted with a linear combination of normal distributions. The component normal distributions corresponding to each linear combination are also shown.

By using the analysis discussed in Section B.2, we find that a linear combination of normal distribution fits to all histograms corresponding to the AFM images in Figure 1.1 with an R-squared value of at least 0.987. The first or left-most distribution for all three figures in Figure 1.2 corresponds to the SiO_2 substrate roughness, centered at ~ 0 nm and with a standard deviation of 0.4-1.2 nm. For the carbon nanotube film deposited with solvent, the second distribution then corresponds to bundles of carbon nanotubes. If we model bundles as cylinders, and we assume the component nanotubes follow 2D packing and are of equal diameter, we can give an estimate the mean bundle size in terms of number of nanotubes n [2], [10], [11].

Table 1.1.: The first eight optimised ratios of 2D packed circle diameter to encompassing circle diameter, given to 3 s.f. (encompassing circle diameter = d , number of packed circles = n , approximate packed circle diameter = d_n).

| n | 2 | 3 | 4 | 5 | 6 | 7 | 8 | 9 |
|---------|------|------|------|------|------|------|------|------|
| d/d_n | 2.00 | 2.15 | 2.41 | 2.70 | 3.00 | 3.00 | 3.30 | 3.61 |

Table 1.1 shows the relationship between the diameter of a bundle and the constituent diameters of up to nine 2D packed carbon nanotubes within that bundle. The second distribution in Figure 1.2a indicates the mean diameter of carbon nanotube bundles is 4.62 nm. Assuming an average carbon nanotube diameter of 1.45 nm, we find a d/d_n packing ratio of 3.19, indicating an average bundle composition of ~ 7 nanotubes in Figure 1.2a.

For the carbon nanotube networks deposited using surfactant in Figure 1.2, we notice that there are two non-SiO₂ distributions present. The mean of the second distribution, the left-most non-SiO₂ distribution, falls below the average height for a single carbon nanotube. This attribute indicates that the distribution either represents broken pieces of individual carbon nanotubes, residual surfactant or other atmospheric contamination resistant to acetone and isopropanol rinsing. This contamination distribution is significantly larger for the carbon nanotube devices which used steam in the deposition process. The presence of this contamination histogram distribution was consistently found for all sampled surfactant-deposited film AFM data, while not present for any of the sampled solvent-deposited films.

From Figure 1.1c, we also see that steam deposited devices have sparsely distributed ~ 10 nm high features visible on their surface which are not present for the other films. These observations may be evidence of trapped water microdroplets on the surface from the steam, or could be from the steam causing surfactant to form persistent features on the surface. The size of this central peak may be useful for determining the extent of contamination in a carbon nanotube film, discussed further in **?@sec-contamination**. Such contamination may or may not have implications for biosensing suitability, but surfactant contamination could certainly have negative effects on biological elements sensitive to surfactant.

The distribution means corresponding to each type of deposition method, averaged across histogram fits from three $2.5\ \mu\text{m} \times 2.5\ \mu\text{m}$ atomic force microscope images, are given in Table 1.2. The carbon nanotube bundle mean is given alongside the number of carbon nanotubes corresponding to the mean height according to 2D packing as given in Table 1.1 and Thanahaichelvan *et al.* [2].

It is noticeable that the location of silicon and contamination distribution means are highly consistent between films. Also notable is a the large decrease in bundle size when surfactant is used in the deposition process. There is also a large standard deviation

Table 1.2.: The mean of histogram distributions across three different samples for carbon nanotube films deposited using various methods, along with the mean sample coverage with bundles and mean proportion of multitubed bundles present. The mean of the carbon nanotube bundle distribution is shown with an estimate of the number of nanotubes that could pack into the mean bundle size via 2D packing.

| | Distribution Mean (nm) | | | Bundle Attributes | |
|---------------------------------|------------------------|---------------|--------------------|-------------------|-------------|
| | Silicon | Contaminant | Bundles (tubes) | % multi-tube | % coverage |
| Solvent deposited | 0.1 ± 2.3 | — | 6.2 ± 3.7 (13) | 78 ± 16 | 35 ± 21 |
| Surfactant deposited | 0.0 ± 0.4 | 1.0 ± 0.4 | 2.0 ± 1.8 (1) | 27 ± 25 | 31 ± 9 |
| Surfactant deposited with steam | 0.0 ± 0.5 | 1.3 ± 0.6 | 2.0 ± 1.2 (1) | 17 ± 17 | 50 ± 11 |

in mean bundle size seen for solvent deposited devices, corresponding to a wide range of bundle sizes present on the atomic force microscope images of the solvent-deposited films.

It is also important to consider that for all figures in Figure 1.1, larger height measurements in the carbon nanotube distribution include surface contamination on the carbon nanotubes as well as bundle-bundle junctions. The distribution may also encompass broken nanotube pieces and some silicon oxide surface contamination at the low end of the range. When considering the proportion of single-tube bundles relative to multi-tube bundles, we exclude heights from the carbon nanotube normal distribution below 1.2 nm, the minimum height of the supplied carbon nanotubes. We also exclude heights above double the distribution mean, to ignore bundle-bundle junctions and surface contamination.

We then compare the proportion of the curve below and above 2.9 nm, the minimum multi-tube bundle size for 1.45 nm diameter nanotubes. By doing so, we get a rough estimate of the proportion of single- to multi-tube bundles present on the surface. We can also compare the total area of the carbon nanotube distribution to the area of the other distributions to get an estimate of the surface coverage by bundles. These values, averaged across the histogram fits from three $2.5 \mu\text{m} \times 2.5 \mu\text{m}$ atomic force microscope images, are given in Table 1.2. It should also be noted that nanotubes undergo some compression from the AFM tip, so these values are possibly underestimates. However, the mean values for surfactant-deposited films are in line with those previously found for IsoNanotubes-S deposited on silicon oxide using alternative analysis methods [8].

In Figure 1.1 and Table 1.2, we see that carbon nanotubes deposited in a surfactant dispersion form bundles which are significantly less wide than the bundles in the film deposited using solvent. However, we also see that despite the presence of surfactant, not all surfactant-dispersed carbon nanotubes are deposited individually. Bundling may occur during the process of deposition onto the substrate, which could disrupt the repulsive forces from the surfactant coating and allow attractive forces to temporarily dominate. The

It is possible that the bundling of surfactant-dispersed carbon nanotubes occurs due to the coffee-ring effect [12], [13]. The coffee-ring effect refers to a build-up of dispersed solid forming around the edges of a dispersion evaporating on a surface. This process occurs due to the dispersion edges being fixed by surface forces, leading to capillary flow outwards to replace liquid evaporating at the edges, bringing solid material along with it. The presence of vapour is known to disrupt this effect [14]. Table 1.2 demonstrates that on average, the presence of steam reduces the number of nanotube bundles present and increases surface coverage, supporting the above hypothesis.

1.2. Electrical Characteristics

1.2.1. Carbon Nanotubes

Each carbon nanotube device fabricated was electrically characterised as described in **?@sec-electrical-characterisation**. Figure Figure 1.3 displays multi-channel measurements of representative devices fabricated as described in **?@sec-fabrication**. To ensure a consistent comparison, each device here was encapsulated with AZ[®] 1518 encapsulation before measurements were taken. The channels which did not exhibit reliable transistor characteristics are not shown. These non-working channels were either short, due to metal remaining on the channel after lift-off, or were very low current, due to a very sparse carbon nanotube network. Devices shown here with a solvent-deposited carbon nanotube network were fabricated prior to Jan 2022; devices with a surfactant-deposited network without steam present were fabricated prior to Jun 2021; devices with a surfactant-deposited network without steam were fabricated prior to Sep 2022.

Consistent subthreshold regime behaviour between channels is desirable for reliable multiplexed biosensing.

1.3. Salt Concentration Sensing with Phosphate Buffered Saline

-nLOF2020 resist being used leads to devices with less drift!!

1.3. Salt Concentration Sensing with Phosphate Buffered Saline

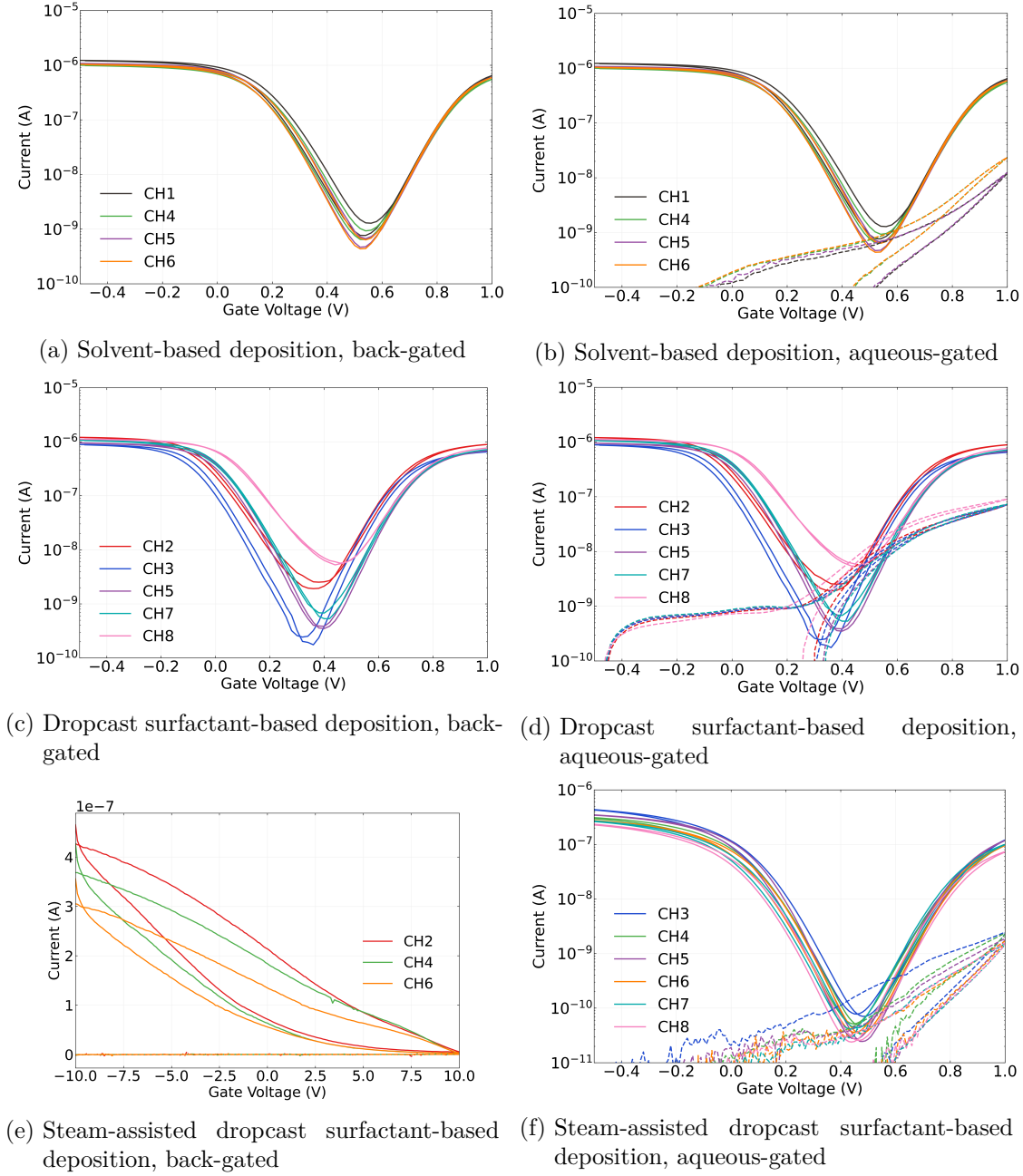


Figure 1.3.: Transfer characteristics of carbon nanotube networks deposited using various methods. 1XPBS was used as the buffer for the liquid-gated measurements here. Source-drain voltage used was $V_{ds} = 100\text{mV}$, with a step size of either 10 or 20 mV used for the sweep.

A. Photolithography

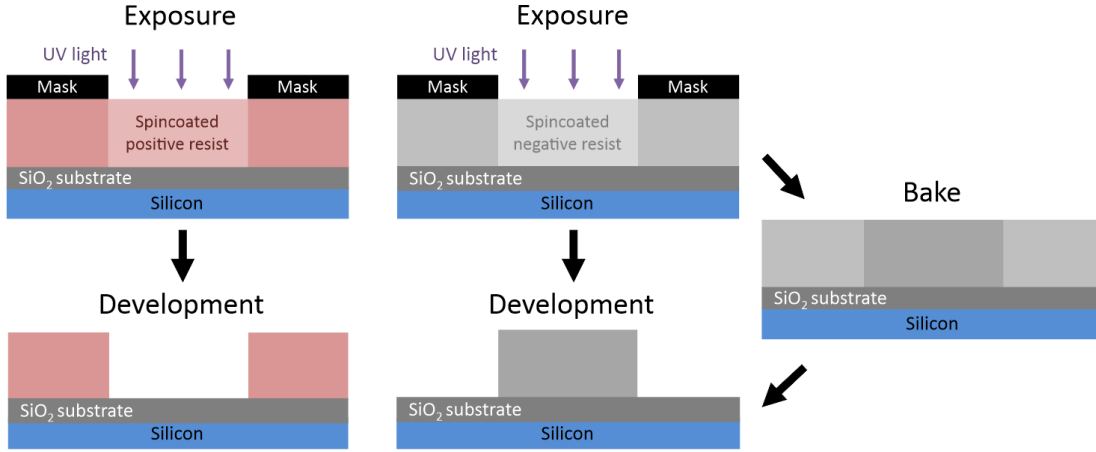


Figure A.1.: A side-view comparison of generic photolithography processes for positive and negative resists in the ideal case. Photolithography with a positive resist requires a single softbake step before exposure, while for negative resists a second baking step is required after exposure (Thicknesses shown not to scale).

This section details some of the standard photolithography procedures used in the device fabrication processes detailed in **sec-fabrication**. Photoresists, also referred to here as “resists”, are UV light-sensitive polymeric resins used for photolithography. Both positive and negative photoresists were used in various fabrication processes. Positive resists are made soluble in alkalines by UV light exposure, meaning exposed areas are removed in the development process. Conversely, negative resists are cross-linked by exposure and a post-exposure bake step. The unexposed areas of the negative resist are then removed in the development process [15]. Figure A.1 gives a visual representation of these differences.

The specific photoresist selected for photolithography depends on the specific use case. The types used in this thesis are positive and negative AZ[®] photoresists (AZ[®] 1518, Microchemicals GmbH; AZ[®] nLOF 2020, Microchemicals GmbH) and SU-8 (SU8-2150, Kayaku Advanced Materials, formerly Microchem). The AZ[®] resists used here have a minimum film thickness of 1.5 μm [15], while the SU8-2150 has a minimum film thickness of 0.5 μm [16]. Positive resists which have not been thermally crosslinked will soften at higher temperatures ($\gtrsim 100^\circ\text{C}$ for AZ[®] 1518), leading to a rounded profile. This is not

A. Photolithography

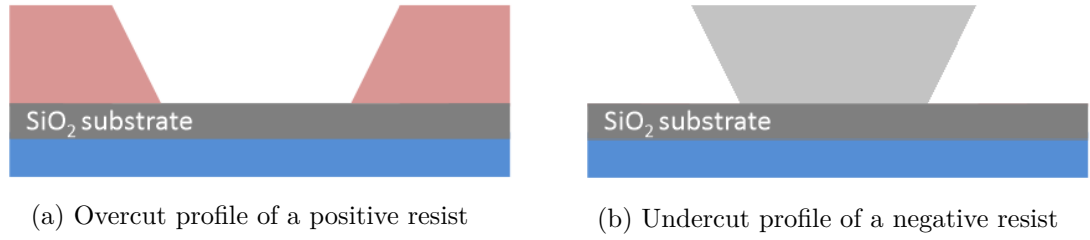


Figure A.2.: Two different resist profiles seen for different types of photoresist. Each profile has had the central region of the substrate exposed to UV light prior to development. The undercut profile is ideal for thin-film metal deposition and subsequent patterned removal, known as “lift-off”.

the case for negative resists, which are more thermally stable [15]. Each resist therefore has a different cross-section profile, as shown in Figure A.2.

If metal deposition is performed on a positive resist, some metal can collect on the outwardly-sloped sidewalls of the resist (see Figure A.2) which forms significant spikes on the edges of the deposited metal upon lift-off. On the other hand, metal cannot collect on top of the inwardly-sloped negative profile sidewalls, which avoids the formation of large edge spikes. Therefore, the negative resist profile is more suited to metal or metal oxide deposition and lift-off processes, though the process is more sensitive to human error due to requiring more processing steps than positive resist [15]. Finally, when it is suitably processed SU-8 is considered to be more stable and biocompatible than other photoresists [17]. It is especially biocompatible when chemically modified via processes such as isopropanol sonication and O_2 plasma treatment [18].

All photolithographic exposure was performed using a Karl Suss MJB3 Contact Aligner with a USHIO super-high pressure 350 W mercury lamp (USH-350DS, Japan). When performing photolithography, the intensity reading from the aligner was 20.8 - 24.2 mW/cm² (Note however that an external photometer reading at 400 nm found an intensity output of 17.2 mW/cm² when the aligner read 21.0 mW/cm²).

In general, photolithography procedures should be performed under yellow lighting, as light wavelengths from 320-450 nm can promote reactions in the photoresist used. Aging of photoresist over time can also significantly affect the photolithography process, and therefore all processes should be re-optimised regularly over time to give the desired result [15]. The range in processing times for some steps of the processes used here are largely due to the effects of aging on the photoresist.

The step-by-step processes for each resist are detailed in the subsequent sections.

A.1. AZ[®] 1518 photoresist

1. Spincoat at a final speed of 4000 rotations per minute (rpm) for 1 minute, with an initial acceleration of 500 rpm/s (notes: clean the substrate with acetone, isopropanol (IPA) and nitrogen before spincoating; use only the minimum amount of photoresist required to fully cover the wafer surface; avoid any gaps or bubbles in the photoresist).
2. Softbake 2-4 minutes at 95°C on the hotplate (2 min for individual devices, 4 min for a quarter wafer)
3. Mask expose for 10-12 s (note: clean mask with acetone/IPA and N₂ dry before use)
4. Develop with 3 parts AZ[®] 326 (2.38 % TMAH metal-ion free developer, Microchemicals GmbH) in 1 part deionised (DI) water for 30-45 s (note: rinse for 10-15 s in one development solution, then perform the rest of the development in clean developer for a cleaner profile; lightly agitate the solution throughout the development process)
5. Rinse device for 30 s in DI water to remove excess developer, then dry under nitrogen

A.2. AZ[®] nLOF 2020 photoresist

1. Spincoat at final speed of 3000 rotations per minute (rpm) for 1 minute, with an initial acceleration of 500 rpm/s (notes: clean the substrate with acetone, isopropanol (IPA) and nitrogen before spincoating; avoid any gaps or bubbles in the photoresist)
2. Softbake for precisely 60 s at 110°C on the hotplate
3. Mask expose for 2.7-3 s (note: clean mask with acetone/IPA and N₂ dry before use)
4. Post-exposure bake for precisely 60 s at 110°C on the hotplate to cross-link exposed resist
5. Develop with 3 parts AZ[®] 326 in 1 part DI water for 60-70 s (note: rinse for 30 s in one development solution, then perform the rest of the development in clean developer for a cleaner profile; lightly agitate the solution throughout the development process)
6. Rinse device for 30 s in DI water to remove excess developer, then dry under nitrogen

A.3. SU8-2150 photoresist

1. SU-8 was diluted in cyclopentanone until viscosity was low enough to spincoat on substrate and then sonicated at 50°C for 3-4 hours (Note: The dilution ratio used was ~1 part SU-8 to 5 parts cyclopentanone. However, the age of the SU-8 may mean that significant evaporation had occurred prior to use, and the amount of SU-8 actually present is underrepresented by this ratio)
2. Spincoat first with a final speed of 500 rpm (acceleration 500 rpm/s) for 10 seconds, followed by spincoating at 4000 rpm (acceleration 7500 rpm/s) for 40 s.
3. Softbake for 10 minutes at 95°C on the hotplate
4. Mask expose for 6-8 s (note: clean mask with acetone/IPA and N₂ dry before use)
5. Post-exposure bake for 10 minutes at 95°C on the hotplate to cross-link exposed resist
6. Develop with SU-8 developer (Kayaku Advanced Materials, formerly Microchem) for 10-15 s, then clean in IPA for 30 s, repeat this step once then dry under nitrogen (note: lightly agitate the solution throughout the development process)

B. Python Code for Data Analysis

B.1. Code Repository

The code used for general analysis of field-effect transistor devices in this thesis was written with Python 3.8.8. Contributors to the code used include Erica Cassie, Erica Happe, Marissa Dierkes and Leo Browning. The code is located on GitHub and the research group OneDrive, and is available on request.

B.2. Atomic Force Microscope Histogram Analysis

The purpose of this code is to return morphology statistics such as height distribution and carbon nanotube coverage/density from atomic force microscope (AFM) images of carbon nanotube networks. The code uses the SciPy optimize package to fit two or three normal distributions to .xyz datasets from AFM images processed in Gwyddion (see [?@sec-afm-characterisation](#)). The number of normal distributions was chosen based on which gave a better quality fit to the .xyz data. It was originally designed by Erica Happe in Matlab, and adapted by Marissa Dierkes and myself for use in Python.

The .xyz data is initially sorted into bins with 0.15 nm size. The bin with the maximum number of counts is set at 0 nm, as this peak represents the mean of the surface roughness of the bare silicon. The fitting parameters m_1 , s_1 , k_1 , m_2 , s_2 , k_2 (as well as m_3 , s_3 , k_3 for three normal distributions) are used in the objective function Equation B.1 when optimising.

$$f(x) = k_1 \exp \left(-\frac{(x - m_1)^2}{2s_1^2} \right) + k_2 \exp \left(-\frac{(x - m_2)^2}{2s_2^2} \right) + \dots \quad (\text{B.1})$$

These fitting parameters represent the mean (m), standard deviation (s) and amplitude (k) of each normal distribution. We can find the initial guess for these fitting parameters by using the histogram data to roughly approximate these values. k_1 is taken as the maximum y-value of the data being fitted, m_1 is set to zero and s_1 is taken as one-third of the difference between m_1 and the x-value of the first datapoint where the y-value is greater than 1% of k_1 . We find the Gaussian given by these values, and subtract it from the existing dataset. We then take k_2 to be the maximum y-value of this modified dataset, and m_1 to be the x-value of the maximum y-value. s_2 is taken as the difference

between m_1 and the x-value of the first datapoint where the y-value is greater than 60% of k_2 . This process is repeated to find k_3 and m_3 , and s_3 is one-third of the difference between m_3 and the x-value of the *last* datapoint where the y-value is greater than 1% of k_3 . In this iterative manner, we find a reasonably good initial guess for our fit. The linear combination of distributions given by our initial guess of parameters is shown by the green dotted line in Figure B.1.

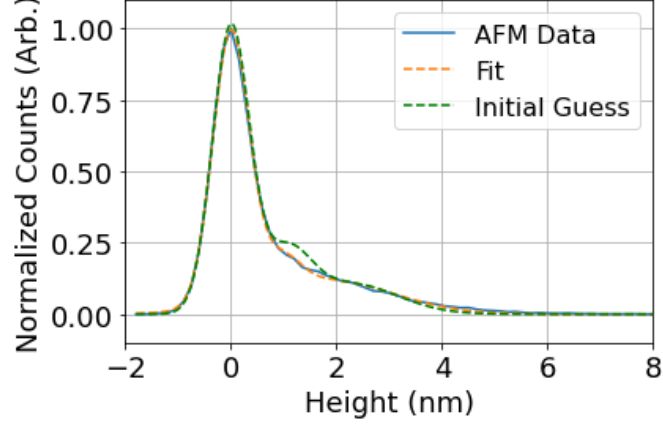


Figure B.1.: Comparing the initial guess and the scipy.optimize fit to the input atomic force microscope histogram

Using the objective function with these fitting parameters in the `scipy.optimize.curve_fit` module, we receive optimised fitting parameters which gave an R-squared value of 0.96 or greater. The linear combination of distributions corresponding to these optimised fitting parameters is shown with the orange dotted line in Figure B.1. By calculating the area under each of the normal distributions found from the fit, we can find the proportion of the surface covered by carbon nanotube bundles relative. The code also allows for discretely binning continuous data from fitted normal distributions and examining the proportion of counts above or below a particular height.

$$f(x) = k_1 \exp\left(-\frac{t}{\tau_1}\right) + k_2 \exp\left(-\frac{t}{\tau_2}\right) + \dots + c \quad (\text{B.2})$$

C. Vapour Delivery System

C.1. Technical Notes

Two LabView Virtual Instruments (VIs) were adapted from pre-existing VIs for operating the mass flow controllers and monitoring vapour flow into the device chamber, as well as monitoring temperature and humidity in the vapour delivery system's manifold. These VIs were named " " A third VI was developed in parallel which combined the first two Virtual Instruments, alongside allowing the sequence of values to control the mass flow controllers.

From Honours report: " " Figure 12 gives the right side of the front panel of the LabView VI sample with vapour.VI, which lets us preset an autonomously-performed vapour sensing sequence. Each row in each array module corresponds to a different step in this sequence. The 'howManySteps' module lets us set how many of these steps are performed. The 'Durations Array' module determines the length of time in seconds each step is performed over. The 'Carrier Flows Array' and 'Dilution Flows Array' modules let us set the carrier flow and dilution flow, respectively, in standard cubic centimetres per minute (sccm) through the gas rig at each step. The carrier flow pushes analyte vapour into the vapour-sensing device chamber, while dilution flow is used to modify the flow behaviour of the analyte vapour entering the chamber. The vapour sensing sequence as depicted in Figure 12 was used for all vapour sensing runs in this investigation. At the end of the sequence, the data collected about the vapour sensing process was saved as an .lvm file. " " "

C.2. Future Improvements

Bibliography

- [1] H. Y. Zheng and N. O.V. Plank. “Facile fabrication of carbon nanotube network thin film transistors for device platforms”. In: *International Journal of Nanotechnology* 14.1-6 (2017), pp. 505–518. ISSN: 14757435. DOI: 10.1504/IJNT.2017.082473.
- [2] Murugathas Thanihaichelvan, Leo A. Browning, Marissa P. Dierkes, et al. “Data on liquid gated CNT network FETs on flexible substrates”. In: *Data in Brief* 21 (Dec. 2018), pp. 276–283. ISSN: 2352-3409. DOI: 10.1016/J.DIB.2018.09.093.
- [3] Murugathas Thanihaichelvan, Leo A. Browning, Marissa P. Dierkes, et al. “Metallic-semiconducting junctions create sensing hot-spots in carbon nanotube FET aptasensors near percolation”. In: *Biosensors and Bioelectronics* 130 (Apr. 2019), pp. 408–413. ISSN: 0956-5663. DOI: 10.1016/J.BIOS.2018.09.021.
- [4] Hong Phan T. Nguyen, Thanihaichelvan Murugathas, and Natalie O.V. Plank. “Comparison of Duplex and Quadruplex Folding Structure Adenosine Aptamers for Carbon Nanotube Field Effect Transistor Aptasensors”. In: *Nanomaterials (Basel, Switzerland)* 11.9 (Sept. 2021). ISSN: 2079-4991. DOI: 10.3390/NANO11092280. URL: <https://pubmed.ncbi.nlm.nih.gov/34578596/>.
- [5] Wim Wenseleers, Igor L. Vlasov, Etienne Goovaerts, et al. “Efficient Isolation and Solubilization of Pristine Single-Walled Nanotubes in Bile Salt Micelles”. In: *Advanced Functional Materials* 14.11 (Nov. 2004), pp. 1105–1112. ISSN: 1616-3028. DOI: 10.1002/ADFM.200400130. URL: <https://onlinelibrary.wiley.com/doi/full/10.1002/adfm.200400130%20https://onlinelibrary.wiley.com/doi/abs/10.1002/adfm.200400130%20https://onlinelibrary.wiley.com/doi/10.1002/adfm.200400130>.
- [6] Maki Shimizu, Shunjiro Fujii, Takeshi Tanaka, et al. “Effects of surfactants on the electronic transport properties of thin-film transistors of single-wall carbon nanotubes”. In: *Journal of Physical Chemistry C* 117.22 (June 2013), pp. 11744–11749. ISSN: 19327455. DOI: 10.1021/JP3113254/SUPPL_FILE/JP3113254_SI_001.PDF. URL: <https://pubs.acs.org/doi/full/10.1021/jp3113254>.
- [7] Chang Liu and Hui Ming Cheng. “Carbon nanotubes: controlled growth and application”. In: *Materials Today* 16.1-2 (Jan. 2013), pp. 19–28. ISSN: 1369-7021. DOI: 10.1016/J.MATTOD.2013.01.019.
- [8] Dusan Vobornik, Maohui Chen, Shan Zou, et al. “Measuring the Diameter of Single-Wall Carbon Nanotubes Using AFM”. In: *Nanomaterials* 13.3 (Feb. 2023), p. 477. ISSN: 20794991. DOI: 10.3390/NANO13030477/S1. URL: <https://www.mdpi.com/2079-4991/13/3/477/htm%20https://www.mdpi.com/2079-4991/13/3/477>.

- [9] Matěj Velický, Adam J Cooper, Peter S Toth, et al. “Mechanical stability of substrate-bound graphene in contact with aqueous solutions”. In: *2D Materials* 2.2 (May 2015), p. 024011. ISSN: 2053-1583. DOI: 10.1088/2053-1583/2/2/024011. URL: <https://iopscience.iop.org/article/10.1088/2053-1583/2/2/024011%20https://iopscience.iop.org/article/10.1088/2053-1583/2/2/024011/meta>.
- [10] R. L. Graham, B. D. Lubachevsky, K. J. Nurmela, et al. “Dense packings of congruent circles in a circle”. In: *Discrete Mathematics* 181.1-3 (Feb. 1998), pp. 139–154. ISSN: 0012-365X. DOI: 10.1016/S0012-365X(97)00050-2.
- [11] Eckard Specht. *The best known packings of equal circles in a circle*. URL: <http://hydra.nat.uni-magdeburg.de/packing/ci/ci.html> (visited on 2023-09-11).
- [12] Robert D. Deegan, Olgica Bakajin, Todd F. Dupont, et al. “Capillary flow as the cause of ring stains from dried liquid drops”. In: *Nature* 1997 389:6653 389.6653 (1997), pp. 827–829. ISSN: 1476-4687. DOI: 10.1038/39827. URL: <https://www.nature.com/articles/39827>.
- [13] R. T. van Gaalen, C. Diddens, H. M.A. Wijshoff, et al. “Marangoni circulation in evaporating droplets in the presence of soluble surfactants”. In: *Journal of Colloid and Interface Science* 584 (Feb. 2021), pp. 622–633. ISSN: 0021-9797. DOI: 10.1016/J.JCIS.2020.10.057.
- [14] Mindy D. Bishop, Gage Hills, Tathagata Srimani, et al. “Fabrication of carbon nanotube field-effect transistors in commercial silicon manufacturing facilities”. In: *Nature Electronics* 2020 3:8 3.8 (June 2020), pp. 492–501. ISSN: 2520-1131. DOI: 10.1038/s41928-020-0419-7. URL: <https://www.nature.com/articles/s41928-020-0419-7>.
- [15] MicroChemicals. *Photoresists AZ and MicroChemicals TI resists*. URL: <https://www.microchemicals.com/products/photoresists.html> (visited on 2023-06-09).
- [16] Kayaku (Microchem). *SU-8 2000 Permanent Negative Epoxy Photoresist / Kayaku*. URL: <https://kayakuam.com/products/su-8-2000/> (visited on 2023-06-30).
- [17] Faris M. Albarghouthi, Nicholas X. Williams, James L. Doherty, et al. “Passivation Strategies for Enhancing Solution-Gated Carbon Nanotube Field-Effect Transistor Biosensing Performance and Stability in Ionic Solutions”. In: *ACS Applied Nano Materials* 5.10 (Oct. 2022), pp. 15865–15874. ISSN: 25740970. DOI: 10.1021/ACSANM.2C04098/SUPPL_FILE/AN2C04098_SI_001.PDF. URL: <https://doi.org/10.1021/acsanm.2c04098>.
- [18] Ziyu Chen and Jeong Bong Lee. “Biocompatibility of SU-8 and Its Biomedical Device Applications”. In: *Micromachines* 2021, Vol. 12, Page 794 12.7 (July 2021), p. 794. ISSN: 2072-666X. DOI: 10.3390/M12070794. URL: <https://www.mdpi.com/2072-666X/12/7/794>.